Journal of The Electrochemical Society, 2022 **169** 060518

Influence of Laser Structuring and Calendering of Graphite Anodes on Electrode Properties and Cell Performance

Lucas Hille,[z] Hans-Christoph Toepper, Charlotte Schriever, Johannes Kriegler, Josef Keilhofer, Marc P. Noecker, and Michael F. Zaeh

Technical University of Munich, Germany; TUM School of Engineering and Design, Department of Mechanical Engineering, Institute for Machine Tools and Industrial Management, 85748 Garching, Germany

In this study, the influence of calendering and laser structuring on the pore structure and electrochemical performance of electrodes is reported. Graphite anodes of varying bulk porosity were micro structured with pulsed laser radiation. Using scanning electron microscopy and energy-dispersive X-ray spectroscopy, laser structuring was found to release superficial pore clogging caused by calendering and to result in binder agglomerates on the electrode surfaces. Structured electrodes showed higher porosities than their unstructured counterparts due to a thickness increase and material removal, but no significant change in the pore size distribution was detected using mercury intrusion porosimetry. Electrochemical impedance spectra of symmetric battery cells revealed increasing ionic resistances and tortuosities for decreasing electrode porosities. Laser structuring significantly reduced the underlying lithium-ion diffusion limitations at all porosity levels. In a discharge rate test, performance deteriorations at high currents were found to be amplified by calendering and could be diminished by electrode structuring. The performance improvements by laser structuring moved towards lower C-rates for stronger compressed anodes. Despite their growth in thickness and porosity, laser structured graphite anodes showed a higher volumetric energy density at high currents than unstructured electrodes, which demonstrates the potential of electrode structuring for highly compressed anodes.

© 2022 The Author(s). Published on behalf of The Electrochemical Society by IOP Publishing Limited. This is an open access article distributed under the terms of the Creative Commons Attribution 4.0 License (CC BY, http://creativecommons.org/licenses/by/4.0/), which permits unrestricted reuse of the work in any medium, provided the original work is properly cited. [DOI: 10.1149/1945-7111/ac725c]

Manuscript submitted March 31, 2022; revised manuscript received May 4, 2022. Published June 13, 2022.

The rising use of portable electronic devices and the electrification of previously motorized vehicles lead to an increasing global demand for lithium-ion batteries (LIBs).[1,2] However, to meet customer requirements in automotive applications, the energy density of LIBs needs further improvement.[3,4] The realization of low electrode porosities through calendering enhances the volumetric energy density of LIBs as it increases the share of lithium-ion storing active material compared to passive components within a battery cell.[5] A high electrode compaction additionally results in enhanced mechanical strength improving the handleability in industrial battery production.[6–9] Calendering yet not only influences the electrodes' physical properties, but also electrochemical characteristics such as the effective ionic conductivity, the solid electronic conductivity[10] and the contact resistance between active material particles.[11] Furthermore, the charge carrier diffusion through the liquid electrolyte within the pore network of an electrode is inhibited at low porosities.[5,12] The effective ion transport restraints resulting from the porous microstructure of the electrode can be described by the tortuosity τ, which is related to the porosity ε by a proportionality factor α via the Bruggeman relation[13,14]

$$\tau = \varepsilon^{-\alpha}. \quad [1]$$

As an approximation for idealized spherical particles of identical size, the proportionality factor α is often assumed to be 0.5. However, previous studies showed that this value does not hold true for most battery electrodes as it underestimates the tortuosity of non-ideal electrode morphologies.[15–17]

The lithium-ion diffusion limitations in highly compressed electrodes can be reduced by microscopic channels in the electrode coatings facilitating ion movement and reducing electrochemical overpotentials.[18–20] Pulsed laser radiation was proven to be a versatile tool for creating such microscopic holes in the electrode coatings.[21,22] LIBs containing structured graphite anodes show an improved discharge capacity at high discharge currents, an accelerated fast charging capability and reduced lithium plating compared to unstructured references.[23] The performance improvements by laser structuring are especially pronounced when applied to graphite anodes with a high mass loading.[23] Furthermore, LIBs with structured anodes exhibited an enhanced lifetime through the reduction of degradation effects in previous studies.[24,25] Since graphite anodes typically show higher diffusion limitations than most cathodes, electrode structuring is especially promising when applied to anodes.[26,27] Nevertheless, performance enhancements were also reported for LIBs containing structured $LiMn_2O_4$ (LMO),[28] $LiCoO_2$ (LCO),[29,30] $LiNi_xMn_yCo_zO_2$ (NMC) [31–33] and $LiFePO_4$ (LFP) cathodes.[22,34] Additionally, it could be shown that the time-consuming electrolyte filling process, which largely contributes to the production costs of LIBs,[35] can be significantly accelerated through electrode structuring.[36–39]

Cell manufacturers typically want to tune the electrode properties for a specific operating range. Hence, for a given electrode loading, the electrode porosity has to be large enough for a high power density yet small enough for a high energy density. This study shows how the degree of calendering influences the electrode properties and how laser structuring addresses the trade-off between high-power and high-energy LIBs. Graphite anodes possessing varying bulk porosities controlled by calendering were structured by short-pulsed laser radiation introducing a directed porosity in the electrodes. Laser scanning microscopy (LSM) and scanning electron microscopy (SEM) were applied to study the unstructured and structured battery electrode surfaces. Energy-dispersive X-ray spectroscopy and mercury intrusion porosimetry were used to characterize the electrodes' material composition and microstructure. Subsequently, the electrodes were incorporated in symmetric and full coin cells and analyzed by electrochemical impedance spectroscopy (EIS) and a discharge rate test, respectively.

Materials and Methods

Slurry mixing.—For anode manufacturing, deionized water (liquid content 48 wt%) and carboxymethyl cellulose (CMC MAC500LC, Inabata, Japan) were premixed for 30 min at 2500 rpm in a disperser (FM 10-SIP, VMA-Getzmann, Germany). The natural graphite (SMGA5, Hitachi, Japan) and carbon black (Super-C65, Timical, Switzerland) mixture were blended with a planetary orbital mixer (Speedmixer DAC 1100.2 VAC-P, Hauschild, Germany), added to the CMC pre-mixture in four equally-portioned steps and mixed for 15 min at 1500 rpm each. Finally, styrene-butadiene rubber (SBR, Zeon, Japan) was added and mixed for 30 min at 600 rpm. For cathode manufacturing, N-Methyl-2-pyrrolidone (NMP 328634, Merck, Germany) (liquid

[z]E-mail: lucas.hille@iwb.tum.de

content 25 wt%) and polyvinylidene difluoride (PVDF Solef 5130, Solvay, Belgium) were premixed for 15 min at 2000 rpm. The NMC (HED NCM-622 DT011, BASF, Germany) and carbon black, which were previously blended with the planetary orbital mixer, were subsequently added in two equally portioned steps and mixed for 10 min at 2000 rpm each. Both slurries were degassed in the planetary orbital mixer at an absolute pressure of 250 mbar and at 600 rpm for 5 min. The material compositions of both electrodes are summarized in Table I.

Coating and drying.—The anode slurry was coated onto a copper current collector foil with a thickness of 10 μm (Cu-PHC, Schlenk, Germany). Using a doctor blade with a gap of 190 μm and a tape casting coater (MSK-AFA-III, MTI, USA), a dry coating thickness of 131 μm was obtained corresponding to a loading of approx. 11.7 mg cm^{-2} (compare Table I). Analogously, the cathode slurry was coated onto an aluminum current collector foil with a thickness of 15 μm (Al-8079, Korff, Switzerland). A dry coating thickness of 90 μm corresponding to a loading of approx. 17.8 mg cm^{-2} (compare Table I) was obtained using a gap of 125 μm. The electrodes were dried in a convection oven (Mehrzweck-Heissluftofen, Bartscher, Germany) for 40 min at 50 °C.

Calendering.—The dried electrode sheets were compacted using a calender with a roll diameter of 400 mm (EA 102, Coatema, Germany) at a maximum line-load of 1000 N mm^{-1} and a roller speed of 0.5 m min^{-1}. The anodes with an initial porosity of 56% and thickness of 131 μm were compressed to three different layer thicknesses (78 μm, 84 μm, 93 μm), resulting in bulk porosities of 19%, 27% and 34%. The cathodes were calendered to a thickness of 60 μm corresponding to a porosity of 32%.

Laser structuring.—Subsequently to calendering, the anodes were micro structured using short-pulsed laser radiation. The laser beam with a central emission wavelength of 1064 nm was provided by a pulsed ytterbium fiber laser source (YLPP-1–150V-30, IPG Photonics, USA), deflected by a galvanometric scan head (Racoon 21, Arges, Germany) and focused by an F-Theta lens (S4LFT0080/126, Sill Optics, Germany) to a focus diameter of approx. 27 μm. The anodes were structured with an average laser output power of 13 W, a processing time of 1.0 ms per drilling, a pulse repetition rate of 550 kHz and a pulse duration of 0.15 ns. The drillings were arranged in a hexagonal pattern with a pitch distance of 120 μm.

Electrode analysis.—Topographic images of the electrode surfaces were captured with a 3D laser scanning confocal microscope (LSM) (VK-X 1000, Keyence, Japan) using the laser confocal height measurement. The topography of the electrodes was analyzed with the accompanying analysis software (MultiFileAnalyzer, Keyence, Japan). The electrode surfaces were further examined using scanning electron microscopy (SEM) (JSM-IT200, Jeol, Japan) and the corresponding image analysis software (Smile View, Jeol, Japan). Chemical element analysis of the electrodes was performed using energy-dispersive X-ray spectroscopy (EDX). All electrode thicknesses were measured with a micrometer screw (Micromar 40ER, Mahr, Germany). The weight of the electrodes was determined with a precision balance (AX26, Mettler Toledo, Switzerland). The porosity ε of the electrodes was calculated from the measured thicknesses d_e, areas A_e and weights m_e by using the mass fractions β_i (compare Table I) and theoretical crystal density values ρ_i of the constituents i:[40]

$$\varepsilon = 1 - \frac{m_e}{d_e \cdot A_e} \cdot \sum_i \frac{\beta_i}{\rho_i} \qquad [2]$$

Mercury porosimetry.—The electrodes' pore structure was analyzed using a mercury porosimeter (Belpore, Microtrac Retsch, Germany) consisting of a low-pressure unit detecting pore sizes between 3 μm and 120 μm and a high-pressure unit detecting pore sizes between 3.6 nm and 15 μm. The sample masses m_{sample} between 0.16 g and 0.21 g were determined by weighing. The dilatometer possessing a filling volume of 430 mm^3 was evacuated, filled with mercury and gradually pressurized. The measurements were started with the intrusion of mercury in the low-pressure unit within a hydraulic pressure range of 12.1 Pa to 450 kPa. Subsequently, the measurement was continued in the high-pressure unit by applying pressures between 100 kPa and 400 MPa. Both experimental steps were performed at a constant temperature of 22 °C with a pressure increase rate of 6–19 MPa min^{-1} and a pressure decrease rate of 8–35 MPa min^{-1}. For the calculation of the pore diameters in dependence of the pressures via the Washburn equation, a constant contact angle of 140° and a constant surface tension of 0.48 Nm^{-1} were assumed for mercury. From the measured pore volume V_{pore}, the coating porosity $\varepsilon_{porosimetry}$ was calculated:[41,42]

$$\varepsilon_{porosimetry} = \frac{V_{pore}}{V_{coating}} = \frac{V_{pore}}{V_{sample} - V_{collector}} = \frac{V_{pore}}{m_{sample}\left(\frac{1}{\rho_{sample}} - \beta_{collector}\frac{1}{\rho_{Cu}}\right)} \qquad [3]$$

The coating volume $V_{coating}$ was determined by subtracting the volume of the current collector foil $V_{collector}$ from the sample volume V_{sample}. Both were derived from the measured sample weight, the respective densities ρ_{sample} and ρ_{Cu} as well as the mass fraction $\beta_{collector}$ in the case of the current collector.

Cell assembly.—Symmetric and full 2032-type coin cells were manufactured for the electrodes' electrochemical characterization and evaluation of the overall cell performance. All cell components were dried under a vacuum of approx. 50 mbar before the cell assembly to eliminate residual moisture. The electrodes and separators were dried in a drying oven (B-585, Büchi, Switzerland) at 120 °C and the remaining cell components were dried in a vacuum dryer (Goldbrunn 1450, Goldbrunn, Germany) at 70 °C for at least

Table I. Characteristics of the single-side coated electrodes.

		Anode	Cathode
Current collector	Material	Copper	Aluminum
	Thickness	10 μm	15 μm
Active material	Material	Graphite	NMC622
	Mass fraction	94 wt%	95.5 wt%
Conductive additive	Material	C65	Carbon black & SFG6L
	Mass fraction	1 wt%	2.25 wt% & 0.75 wt%
Binder additive	Material	CMC & SBR	PVDF
	Mass fraction	2 wt% & 3 wt%	1.5 wt%
Loading		11.7 mg cm^{-2}	17.8 mg cm^{-2}
Theoretical areal capacity		3.9 mAh cm^{-2}	2.9 mAh cm^{-2}

Table II. Symmetric and full cell configurations manufactured for this study; in the labeling, the letters "A" and "C" specify anode and cathode, respectively, and the indices indicate the electrodes' initial porosities before structuring in percent and their condition ("S" for structured and "R" for the unstructured reference).

	Symmetric cells					Full cells			
Reference	$A_{19R}A_{19R}$	$A_{27R}A_{27R}$	$A_{34R}A_{34R}$	$A_{56R}A_{56R}$	$C_{32R}C_{32R}$	$A_{19R}C_{32R}$	$A_{27R}C_{32R}$	$A_{34R}C_{32R}$	$A_{56R}C_{32R}$
Structured	$A_{19S}A_{19S}$	$A_{27S}A_{27S}$	$A_{34S}A_{34S}$	$A_{56S}A_{56S}$	–	$A_{19S}C_{32R}$	$A_{27S}C_{32R}$	$A_{34S}C_{32R}$	$A_{56S}C_{32R}$

12 h each. The coin cells were assembled in a glove box (GS MEGA E-LINE, GS Glovebox, Germany) in an argon atmosphere ($c_{H20} < 0.01$ ppm, $c_{O2} < 0.01$ ppm). For the full coin cells, the anode (diameter 15 mm) and cathode (diameter 14 mm) were separated by a glass fiber separator (diameter 16 mm) (Type 691, VWR, USA) and assembled with two metal spacers of a total thickness of 1.5 mm. The separator was soaked with 100 µl electrolyte (LP572, BASF, Germany) containing 1 M lithium hexafluorophosphate ($LiPF_6$) conducting salt dissolved in ethylene carbonate (EC) and ethyl methyl carbonate (EMC) solvent with a mass fraction of 3:7 and 2 wt% vinylene carbonate (VC). The symmetric cells were assembled analogously to the full cells. However, identical electrodes were paired and 100 µl non-intercalating electrolyte for blocking conditions was used, the latter consisting of 0.01 M tetrabutylammonium perchlorate dissolved in EC:EMC with a volume fraction of 3:7. An electrolyte conductivity κ of 327 µS cm^{-2} was measured at 25 °C using a conductivity meter (Seven2Go, Mettler Toledo, Germany). For both, full and symmetric coin cells, four cells were assembled per configuration. The resulting cell configurations are summarized in Table II.

Potentiostatic electrochemical impedance spectroscopy.—Symmetric coin cells were investigated with electrochemical impedance spectroscopy (EIS). The measurements were performed at 25 °C with a potentiostat (VSP-3e, Bio-Logic SAS, France). Ten logarithmically distributed measurement points per decade were recorded in a frequency range from 1 MHz to 10 mHz at an alternating excitation voltage with an amplitude of 10 mV rms around the open circuit voltage (OCV). The spectra were analyzed using a previously-reported transmission line model for symmetric cells under blocking conditions.[26,43–46] By fitting the expression

$$Z_{el} = \sqrt{\frac{R_{ion}}{Q\,(i\omega)^{\gamma}}}\,\coth\left(\sqrt{Q\,(i\omega)^{\gamma}\,R_{ion}}\right) \qquad [4]$$

to the obtained impedance spectra with a truncated Newton algorithm from the Python library SciPy, values for the ionic resistances R_{ion} were obtained. Furthermore, Eq. 4 features the angular frequency ω, a constant phase exponent γ and Q, which is related to the electrode capacitance. With R_{ion}, the ionic conductivity κ of the electrolyte, the cross-sectional areas A and the thicknesses d of the electrodes, the MacMullin number

$$N_M = \frac{\kappa}{\kappa_{eff}} = \frac{R_{ion}\cdot A\cdot\kappa}{d} \qquad [5]$$

can be calculated.[43] With the empirical relation[13,15,43]

$$N_M = \frac{\tau}{\varepsilon}\,, \qquad [6]$$

the tortuosity can be calculated from the ionic resistance by rearranging Eqs. 5 and 6:

$$\tau = N_M\cdot\varepsilon = \frac{R_{ion}A\,\kappa}{2\,d}\cdot\varepsilon \qquad [7]$$

In the formula, the ionic resistance is divided by an additional divisor of 2, accounting for the added impedance of two identical electrodes incorporated in the symmetric cells.[26,43]

Formation and rate capability tests.—The formation and rate capability tests of the full coin cells were conducted in a heating chamber (ED-115, Binder, Germany) at 25 °C with a battery testing system (CTS, BaSyTec, Germany). For the formation, three charge and discharge cycles were performed at a constant current (CC) of 0.2 C between 2.9 V and 4.2 V. The third charging cycle was followed by a constant voltage (CV) phase at 4.2 V until the current dropped below 0.05 C. During cycling, the cells were charged at CC to the upper cutoff voltage of 4.2 V, followed by a constant voltage (CV) phase until the current dropped below 0.05 C. The cells were discharged at CC-rates varying between 0.1 C and 5 C until a minimum voltage of 2.9 V was reached. The complete procedure is shown in detail in Table A·I in the Appendix. The C-rates were calculated using the cells' absolute capacities of the last discharge cycle of the formation. The capacities of the cells between 4.1 mAh and 4.5 mAh were normalized to the capacity obtained in the first discharge cycle at 0.1 C for each cell to allow comparability at deviating cell capacities caused by loading fluctuations in the cathodes. A limitation of the initial capacities by the anodes can be excluded due to the high ratio of negative to positive electrode capacity (compare Table I).

Post-mortem analysis.—After the rate capability test, the full coin cells were discharged at CC of 0.1 C until the voltage dropped to 2.9 V followed by a CV discharging at 2.9 V until the current dropped below 0.05 C. Subsequently, the cells were opened in a glove box (MB200MOD, M.Braun, Germany) in an argon atmosphere ($c_{H20} < 0.1$ ppm, $c_{O2} < 0.1$ ppm) and the anode thicknesses were measured using a micrometer screw (Micromar 40ER, Mahr, Germany).

Results and Discussion

Electrode morphology, thickness and porosity.—The electrodes resulting from various calendering degrees and subsequent micro structuring were initially analyzed by SEM (see Fig. 1), revealing significant differences. The uncalendered configuration A_{56R} showed a coarse morphology with pores opening on the electrode surface. In contrast, in the calendered reference electrode configurations A_{34R}, A_{27R} and A_{19R}, a clogging of surface pores intensifying with decreasing porosity was evident from the SEM images. Although particle deformations seemed to take place at the surface due to calendering, no particle cracks were observable, even at high compressive forces. This is attributed to the mechanically soft graphite particles.

The SEM images in the lower row of Fig. 1 revealed a tapered geometry of the laser structured channels showing only minor deviations over the different anode porosities. According to LSM measurements (compare Fig. 2), the drillings possessed an upper hole diameter of approx. 39 ± 10 µm and depth of 69 ± 9 µm. The standard deviation was roughly as large as the active materials particle diameter as commonly observed in laser structuring of graphite anodes.[21]

Interestingly, also the areas not directly penetrated by the laser beam exhibited less superficial pore clogging in the structured and calendered electrodes than in the unstructured counterparts. The behavior is visualized at the example of the configurations A_{27R} and A_{27S} in Fig. 3a and indicates an extended heat affected zone by laser structuring resulting in material expansion. Furthermore, the selective

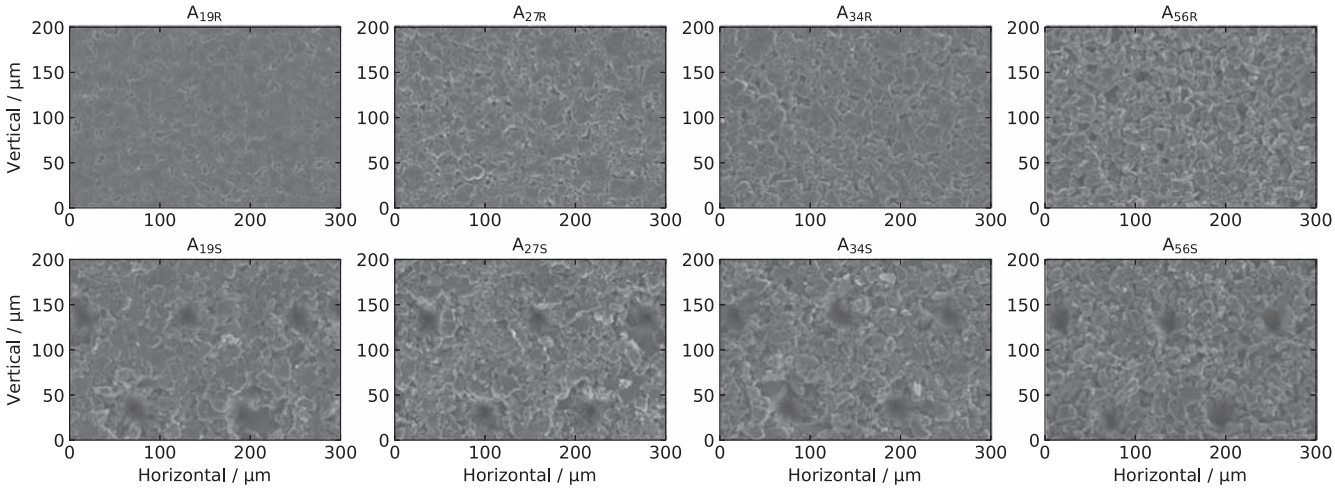

Figure 1. Top-view SEM images of the reference (top row) and structured (bottom row) anode surfaces with initial porosities increasing from the left to the right. In the labeling of the configurations, the number in the subscript refers to the initial porosity before laser structuring and R and S stand for reference and structured condition, respectively.

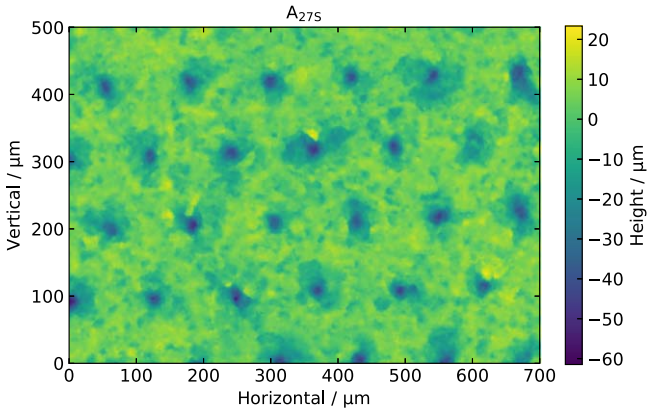

Figure 2. Electrode surface morphology of configuration A_{27S} obtained using LSM.

ablation of the binder additives, which possess a lower evaporation temperature than the graphite,[47,48] could have contributed to the opening of superficial pores. Since CMC is the only component of the anodes containing sodium, an EDX analysis with respect to the material was performed to analyze the binder distribution on the anode surface. EDX maps of pristine CMC (compare Fig. A·1b) confirmed the sodium signal to correlate to the binder. Figure 3b shows a circular accumulation of sodium around the holes at a distance of approx. 30–50 µm to the crater rims. A closer look at the regions reveals star-like shaped particles (compare Fig. 3c), which were identified as CMC due to the detected sodium (compare Fig. 3d). The deviation of the particle shape from the filament structure of CMC in pristine condition (compare Fig. A·1a) might be due to a re-deposition and re-crystallization of the CMC on the electrode surface subsequent to laser structuring. The oxygen signal showed a similar distribution as the sodium signal since CMC is the only electrode component containing oxygen (not shown). Besides that, no further changes were observed in the EDX maps.

As expected from Eq. 2, the reference electrodes showed a porosity decrease with the thickness reductions by calendering (compare Fig. 4). Laser structuring caused a pronounced porosity increase of the electrodes due to the ablation of material by the laser radiation resulting in a mass reduction of the electrodes (compare Eq. 2). It is assumed that the material fractions of graphite, binder and conductive additive in the electrode were not altered significantly by laser structuring. Thus, the channels in the structured electrodes are adding to the bulk porosity, which partly explains the high porosities in comparison with the reference electrodes. Yet, the mass reduction of approx. 3–5%, which was determined by weighing of the electrodes, cannot solely explain the porosity increase of approx. 8–10% in the laser structured and calendered electrodes. Furthermore, the structured anodes showed higher thicknesses of approx. 7.0 –10.5 µm in comparison to their unstructured counterparts, intensifying the porosity increase (compare Eq. 2). The thickness growth was predominantly present in the calendered electrodes and structuring only had a negligible influence on the thickness of the non-calendered electrodes (A_{56}). A potential re-deposition of ablated material onto the electrode surfaces contributing to the thickness increase of the structured electrodes can be ruled out since the effect would have similarly occurred in non-calendered electrodes and very few residual particles were observed in the microscopy images of the structured electrode surfaces (compare Figs. 1 and 2). Also, no pronounced elevations of the crater rims, which could result from particle re-depositions, were evident from the LSM analysis of the electrode surfaces (compare Fig. 2). Hence, the thickness increase by laser structuring is assumed to be a spring-back effect of the compressed electrode particles induced by the heat input of the laser radiation. The material of the electrodes, especially the binder, presumably expanded abruptly upon the laser irradiation (see discussion above) and thus released tensions introduced into the coatings by the calendering process.

In order to evaluate the effect further, mercury intrusion measurements were performed for each anode configuration. From Fig. 5, it becomes evident that each calendering degree correlated with a distinct pore structure. However, among a given porosity, laser structuring did not result in a shift of the prevalent microstructures' pore size. Hence, the electrodes' overall porosity increase can be attributed to the void space introduced into the coating by laser structuring as well as the simultaneous particle expansion. According to Eq. 3, the porosity of each electrode configuration was calculated from the intrusion measurements (compare Table III). With the exemption of A_{19S} and A_{34R}, the values showed only slight deviations to the porosities obtained via Eq. 2 (compare Fig. 4) as previously observed by Meyer et al.[49] The difference can be attributed to particle compressions and pores inaccessible for mercury.

Ionic resistance and electrode tortuosity.—The eight graphite anode configurations representing four porosity levels in the reference and laser structured state were incorporated into symmetric coin cells and analyzed with EIS. Additionally, NMC cathodes, which served as cathodes in the discharge rate tests shown below, were evaluated as a benchmark. Exemplary Nyquist plots of the obtained impedance spectra for the different symmetric cell

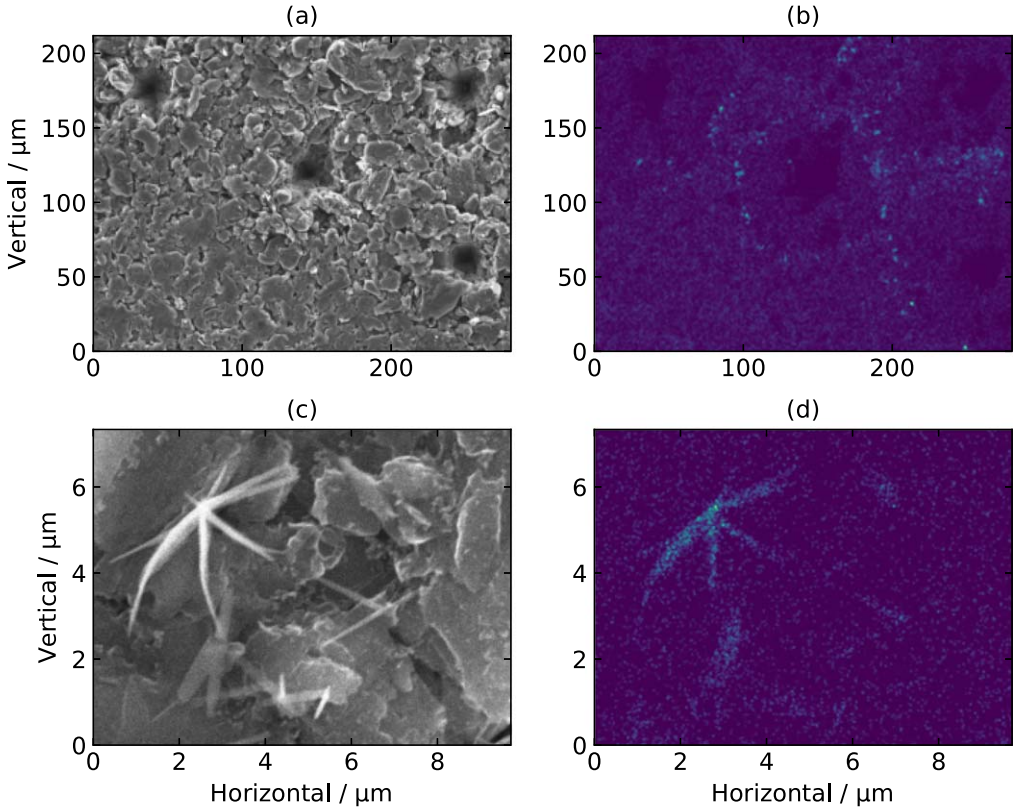

Figure 3. SEM images and EDX maps of A_{27R} and A_{27S} (a) SEM image of the border between structured (top right) and reference (bottom left) electrode surface and (b) the corresponding EDX map of sodium. (c) Zoom-in SEM image of a CMC particle and (d) the corresponding EDX map of sodium in normalized counts.

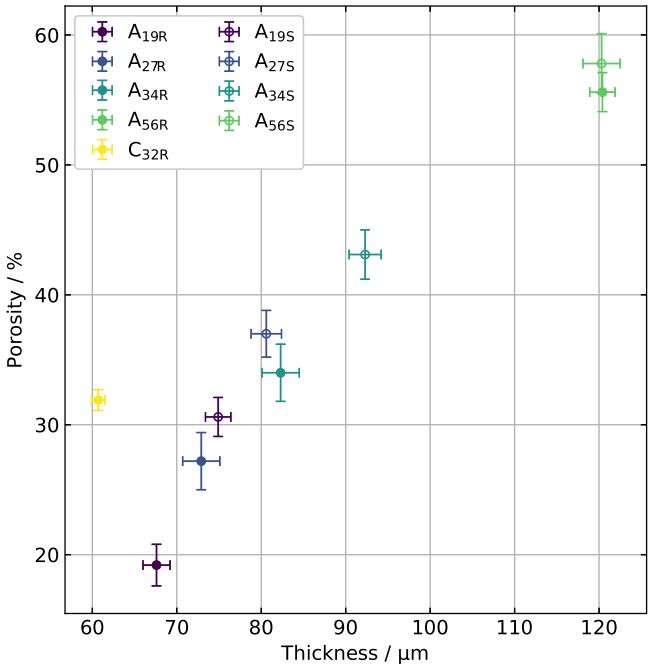

Figure 4. Porosities of electrodes against the respective coating thicknesses. In the labeling of the configurations, the number in the subscript refers to the initial porosity before laser structuring and R and S stand for reference and structured condition, respectively. Average and standard deviation result from twelve electrodes per configuration.

configurations are shown in Fig. 6. Horizontal and vertical shifts in the impedance spectra of the unstructured electrodes depending on the porosity can be observed. The Nyquist plots of the structured

Table III. Porosities $\varepsilon_{\text{porosimetry}}$ obtained from the Mercury intrusion measurements using Eq. 3.

	A_{19}	A_{27}	A_{34}	A_{56}
A_R	17%	25%	42%	53%
A_S	43%	39%	45%	61%

electrodes, in contrast, did not show a strong dependence of the porosity. Hence, laser structuring resulted in impedance shifts of the structured electrodes compared to their respective reference configurations. As can be seen from Fig. 6, the measured impedance data and the respective fits of Eq. 4 show a good coincidence for all cells.

From Fig. 7, a pronounced increase of the average ionic resistances of the reference anode configurations with decreasing porosity is observable. Laser structuring allowed reducing the ionic resistance of the cells significantly for all initial porosity levels. The effect was most pronounced in the configuration $A_{19S}A_{19S}$, in which a reduction of the ionic resistance by nearly an order of magnitude in comparison to the respective reference configuration $A_{19R}A_{19R}$ was observed. Symmetric cells consisting of unstructured NMC cathodes showed a lower ionic resistance than the reference anode configurations, but higher values than the structured anodes (except $A_{19S}A_{19S}$), which is in agreement with previously reported studies.[26,27]

The tortuosities for all cell configurations calculated with Eq. 7 as well as fits of the Bruggeman relation (compare Eq. 1) for the reference and structured anode configurations are depicted in Fig. 8 against the electrode porosities. While fitting for the structured anodes ($\alpha_S \approx 0.6$, dashed line in Fig. 8) yielded a Bruggeman exponent comparable to the approximation for spherical particles ($\alpha = 0.5$, solid line in Fig. 8), a significantly higher exponent was obtained for the reference anodes ($\alpha_R \approx 1.7$, dotted line in Fig. 8). The value for α_R lies in the range of previously reported Bruggeman exponents for graphite anodes determined via 3D particle

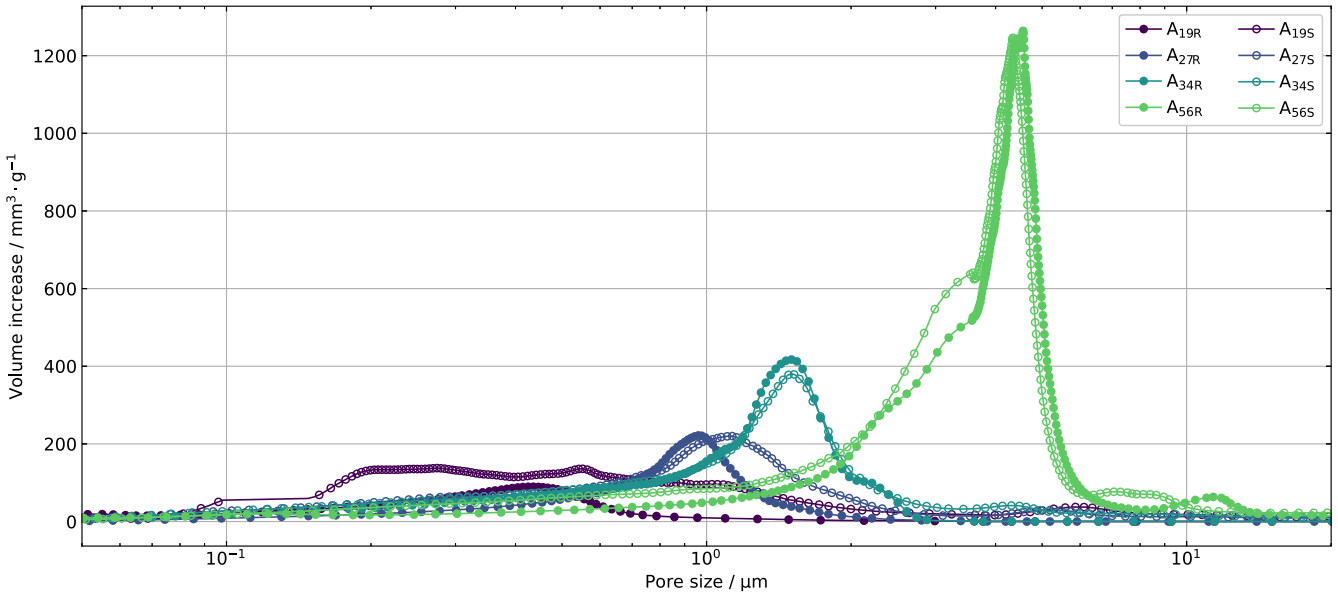

Figure 5. Pore size distributions of graphite anodes. In the labeling of the configurations, the number in the subscript refers to the initial porosity before laser structuring and R and S stand for reference and structured condition, respectively.

reconstruction [50] and differential effective medium approximation,[51] but differs from values reported by Landesfeind et al., who were using the same electrochemical approach as in this work.[43] The deviations are ascribed to the application of a generalized Bruggeman relation featuring a pre-factor by Landesfeind et al. as well as differences in the particle shapes, sizes and electrode compositions.[43] The high absolute tortuosities obtained in this study are attributed to the used binder additives (CMC & SBR), which were previously shown to cause high tortuosities.[52]

Over the whole porosity range, the tortuosity was significantly reduced by laser structuring. The structured electrodes not only exhibited a lower tortuosity than their unstructured counterparts, but also lower values than unstructured configurations with a higher initial (and comparable actual) porosity, e.g. $\tau_{A21S} < \tau_{A34R}$. Hence, the tortuosity reduction cannot solely be ascribed to the earlier discussed porosity increase by laser structuring (compare Fig. 4), but primarily to a facilitated ion diffusion caused by the microscopic channels in the electrode coatings.[18–20] Furthermore, the opening of superficial pores by laser structuring as discussed above (compare Fig. 3) improves the ion diffusion, as the ionic current is the highest at the electrode surface.[46] The selective ablation of binder and other additives close to the electrode surface can already result in an enhanced electrochemical performance of LIBs due to the opening of pores.[53] Interestingly, laser structuring also resulted in a significant tortuosity decrease in electrodes which were not calendered at all (A_{56}). This indicates that the platelet-like shape of the graphite particles poses a high resistance to the ion diffusion even at high porosities and without superficial pore clogging. Furthermore, the selective laser ablation of binder presumably contributed to the tortuosity decrease in the un-calendered electrodes as the binder strongly influences the effective ionic transport properties of porous electrodes.[52,54] While the tortuosities of the reference anodes lie well above the values of the NMC cathodes, all structured anodes exhibited lower tortuosities than the cathodes. This emphasizes that the diffusion-limiting nature of the graphite anodes in many cell configurations can be compensated by laser structuring.[26] The impact of the electrode porosity and structure on the performance of LIBs will be discussed in the following.

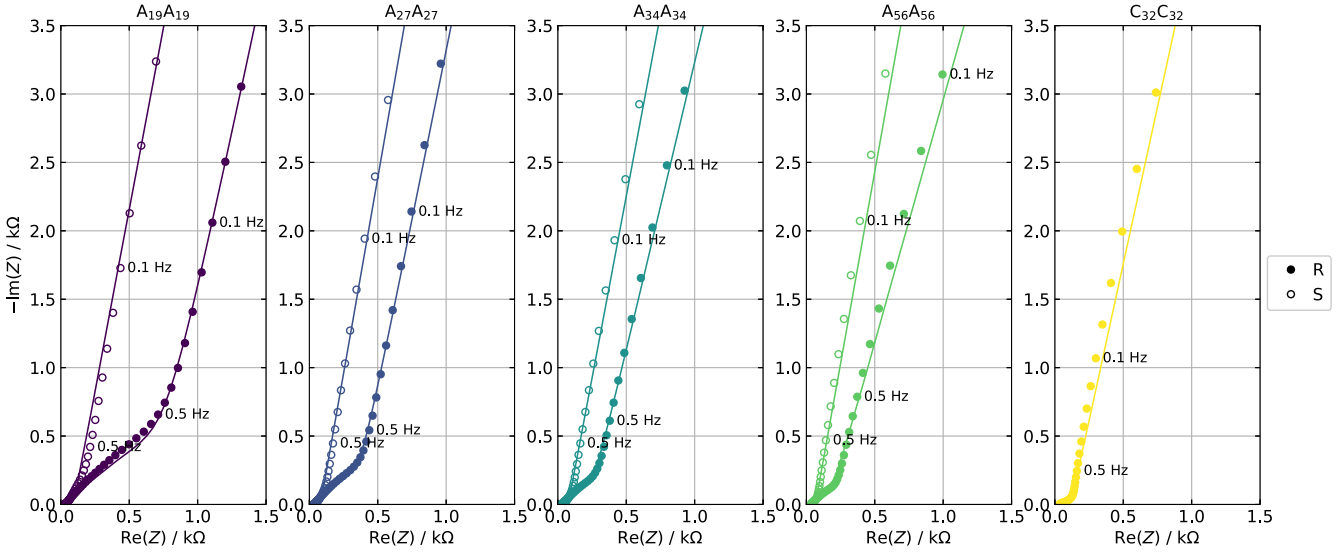

Figure 6. Exemplary Nyquist plots of symmetric cells featuring fits of Eq. 4. In the labeling of the configurations, the number in the subscript refers to the initial porosity before laser structuring and R and S stand for reference and structured condition, respectively.

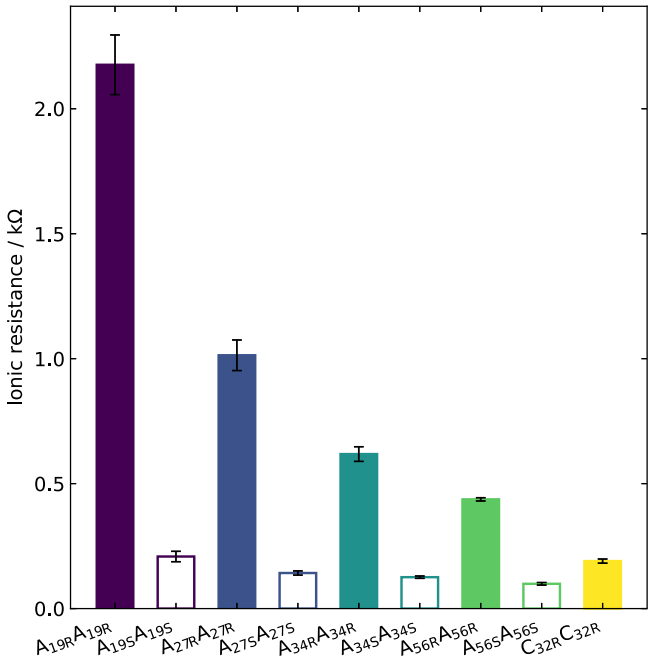

Figure 7. Ionic resistance of symmetric cells obtained from fitting of Eq. 4 to the respective experimental impedance data. In the labeling of the configurations, the number in the subscript refers to the initial porosity before laser structuring and R and S stand for reference and structured condition, respectively. Average and standard deviation result from four cells per configuration.

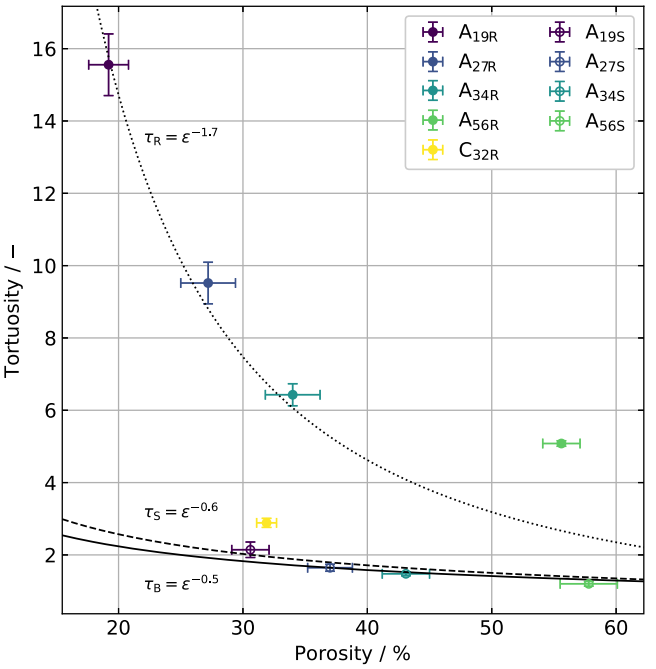

Figure 8. Tortuosity of electrodes against the respective coating porosity featuring fits of Eq. 1 for the reference ($\tau_R = \varepsilon^{-1.7}$) and structured ($\tau_S = \varepsilon^{-0.6}$) anodes as well as the ideal Bruggeman relation ($\tau_B = \varepsilon^{-0.5}$). In the labeling of the configurations, the number in the subscript refers to the initial porosity before laser structuring and R and S stand for reference and structured condition, respectively. Average and standard deviation result from four cells per configuration.

LIB rate performance.—To evaluate the respective influence of electrode compression and laser structuring on the performance of LIBs, a discharge rate test was conducted. Figure 9a displays the discharge capacities of all cell configurations at C-rates between 0.1 C and 5 C. The discharge capacities obtained at C-rates larger than 1 C were generally higher for LIBs with anodes of a lower compaction level. LIBs of the reference cell configurations showed a pronounced capacity decrease within the cycles of intermediate to high C-rates, e.g., $A_{19R}C_{32R}$ at 2 C. The effect intensified and occurred at lower C-rates with decreasing porosity, indicating diffusion limitations. The capacity fade during cycles of the same C-rate was eliminated by electrode structuring of the non-calendered electrodes and decreased to a lower extent for the calendered electrodes indicating a reduction of overpotentials in the anodes through laser structuring. A capacity loss of the unstructured cells with low porosity, e.g., $A_{19R}C_{32R}$ or $A_{27R}C_{32R}$, was observed in 0.1 C check-up cycles conducted at the end of the rate test. The degradation is ascribed to an irreversible loss of the lithium inventory caused by lithium plating on the anode surfaces as previously described by Kriegler et al.[24] Although only moderate C-rates of up to 1 C were applied for charging (compare Table A·I), lithium plating is expected to have occurred due to the low porosities and high tortuosities (compare Fig. 8). The irreversible capacity loss observed in the check-up cycles was reduced by laser structuring to less than 3.5% for all configurations. This is ascribed to a mitigation of cell-internal overpotentials and a correlated decrease of lithium-ion concentration gradients in the electrolyte.[19,55] Electrode structuring resulted in a pronounced increase of the obtained discharge capacities for all porosities. In Fig. 9b, the discharge capacity differences of the last cycle at each C-rate between structured and reference cells are displayed. The discharge capacity improvement due to laser structuring rises with increasing discharge currents up to a specific limit as observed in previous experiments.[24,55,26] The effect is correlated to a reduction of cell-internal overpotentials resulting from diffusion.[19,20] At very high C-rates, where other limitations such as the solid-state diffusion or ion diffusion in the cathodes start to dominate,[20,26] the gap between structured and reference cells decreases. From Fig. 9b, it becomes evident that the discharge capacity improvement by laser structuring moves towards lower C-rates when going to lower anode porosities. This indicates that the diffusion-limited C-rate, i.e., the C-rate at which significant capacity decline occurs,[56] scales inversely with the anode porosity and can be shifted to higher values by laser structuring. Furthermore, the maximum capacity improvement by laser structuring increases from approx. 20% in the cells with uncalendered electrodes ($A_{56S}C_{32R}$) to 25% for the cells with the most compacted anodes ($A_{19S}C_{32R}$).

Considering that the porosity and thickness of A_{19S} match best with the one of A_{27R} and likewise A_{27S} with A_{34R} (compare Fig. 4), it is noteworthy that even when comparing these structured and reference cells with different calendering levels, the structured cells still outperform the unstructured ones in terms of discharge capacity. The behavior becomes apparent when examining the volumetric capacity density of the cell configurations, i.e., the capacity obtained at a certain C-rate divided by the coating volume of the respective electrode configuration. Figure 10 displays the capacity densities at a discharge current of 4 C and shows that LIBs containing structured electrodes possess a higher volumetric capacity density than the reference configurations. Hence, electrode structuring significantly enhanced the discharge performance, although the laser process increased the electrode thicknesses. Figure 10 again underlines that the ion diffusion facilitation by laser structuring exceeds the performance improvements expected from a pure increase in bulk porosity. Furthermore, a porosity-dependent "sweet spot" in terms of capacity density is evident from Fig. 10. For the examined cells, it lies at a porosity between 27% and 34% in the unstructured configurations and moved towards lower initial (27%), yet higher actual (37%) anode porosities in the structured configurations at 4 C. The determination of a porosity-dependent C-rate, at which the highest capacity retention improvement can be observed, augments the findings by Dubey et al., who reported a performance increase of laser structured low porosity electrodes in comparison to unstructured and uncalendered electrodes, respectively.[23]

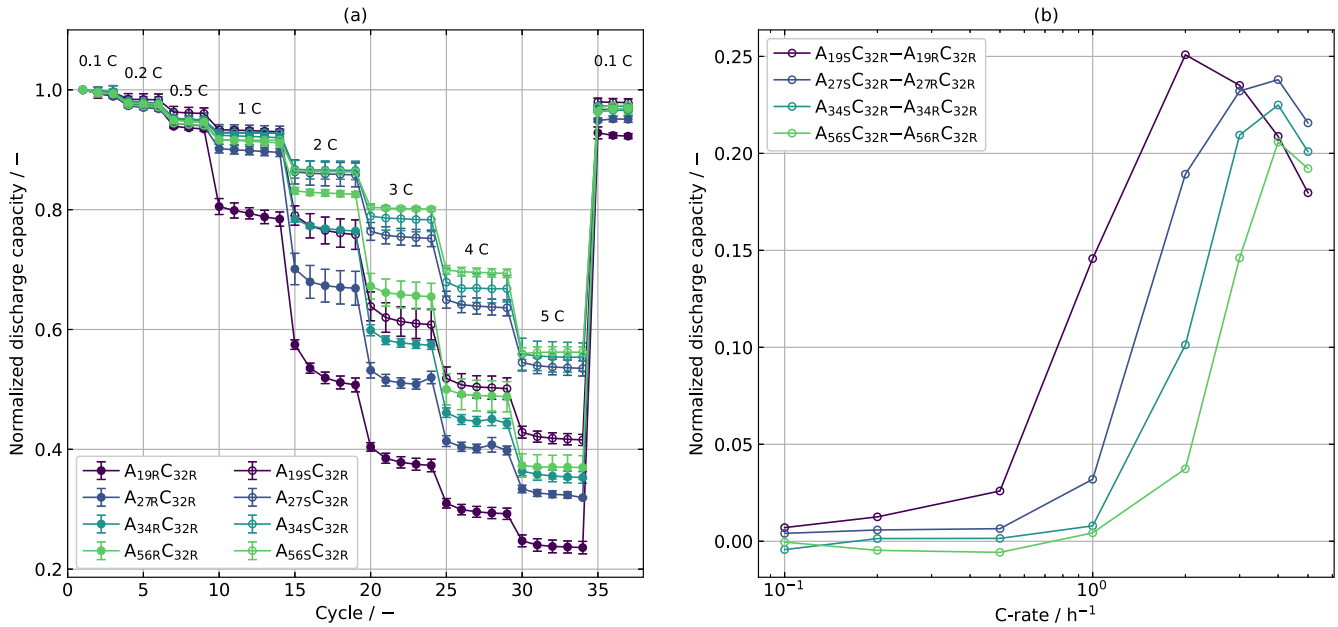

Figure 9. (a) Capacities of full cells obtained in a discharge rate test with 3 to 5 cycles at C-rates ranging from 0.1 C to 5 C. The values are normalized to the capacity obtained in the first discharge cycle at 0.1 C for each cell. In the labeling of the configurations, the number in the subscript refers to the initial porosity before laser structuring and R and S stand for reference and structured condition, respectively. Average and standard deviation result from four cells per configuration. (b) Discharge capacity differences of structured and reference cells of each initial porosity at the last cycle of every discharge rate.

The influence of the electrode microstructure on the attainable energy and power density is visualized in a volumetric Ragone plot in Fig. 11. The figure summarizes how the restrictions of current state-of-the-art electrode materials can be addressed by laser structuring as the maximum energy density at high power densities was improved for all calendered configurations by electrode structuring. This is due to the discharge capacity increases and a higher mean voltage level in LIBs with structured electrodes as previously reported by Kriegler et al.[24] In addition to the above discussed porosity-dependent sweet spot, a maximum energy density depending on the current, i.e., the applied C-rate, is evident. Since the results shown in Fig. 11 depend on the electrode volume, the electrode thicknesses were measured in a post-mortem analysis subsequent to the discharge rate test. Figure 12 shows a thickness increase due to cycling for all electrodes, which is ascribed to a residual lithiation of the graphite anodes.[57] The reference electrodes exhibited a larger thickness growth in comparison to the structured electrodes possessing a higher initial thickness due to the laser

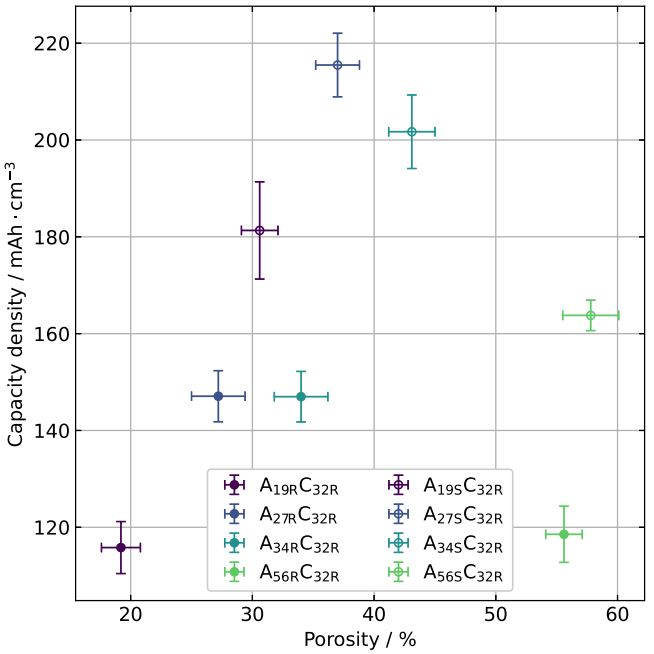

Figure 10. Discharge capacity densities of full cells obtained by dividing the discharge capacity of the last cycle at 4 C by the respective coating volumes against the respective coating porosities. In the labeling of the configurations, the number in the subscript refers to the initial porosity before laser structuring and R and S stand for reference and structured condition, respectively. Average and standard deviation result from four cells per configuration.

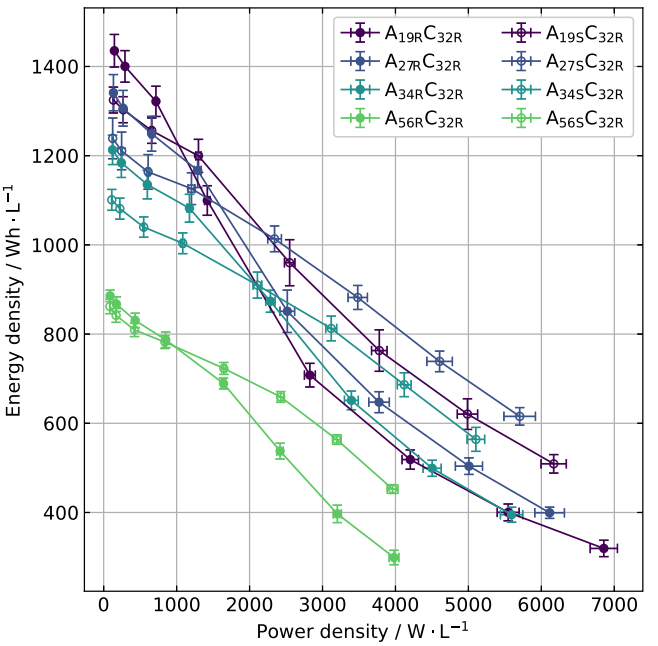

Figure 11. Ragone plots for the volumetric energy density of full cells obtained from the discharge capacities of the last cycle at each C-rate. The normalization refers to the coating volume of the anodes. In the labeling of the configurations, the number in the subscript refers to the initial porosity before laser structuring and R and S stand for reference and structured condition, respectively. Average and standard deviation result from four cells per configuration.

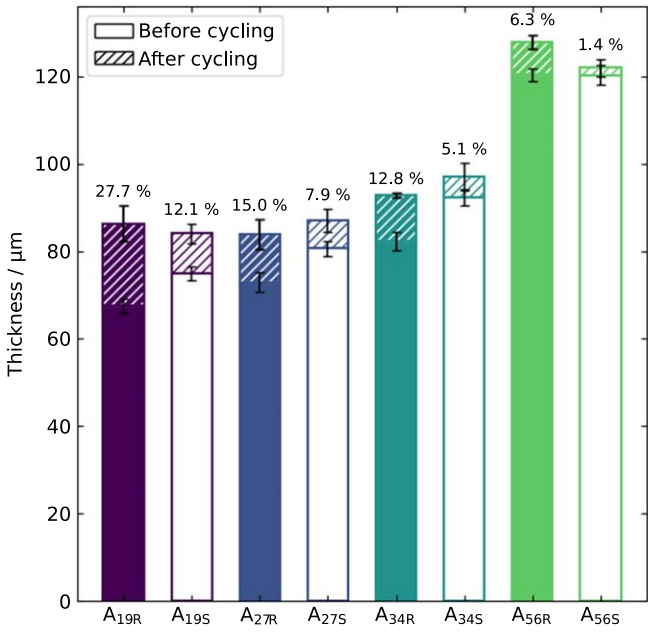

Figure 12. Thicknesses of the graphite anode coatings before cycling (plain bars) and after cycling (hatched bars) with percentage change annotated for each configuration. In the labeling of the configurations, the number in the subscript refers to the initial porosity before laser structuring and R and S stand for reference and structured condition, respectively. Average and standard deviation result from four cells per configuration.

structuring (compare Fig. 4). The void space introduced into the electrode coatings by structuring minimizes the volume expansion of the electrodes during cycling as previously observed for silicon-graphite anodes.[58] The behavior intensifies the positive effect of electrode structuring on the volumetric energy densities and power densities shown in Fig. 11, which were deduced from the electrode thicknesses prior to cycling. Conclusively, electrode structuring is a promising approach for an application-oriented design of LIBs. By alleviating the trade-off between a high energy density and high operational powers, electrode structuring enhances the suitability of LIBs for demanding applications like electric mobility.

Conclusion and Outlook

In this study, the effect of laser structuring on graphite anode properties such as topology, porosity, microstructure and tortuosity as well as on the overall cell performance was quantified. To achieve this, graphite anodes of different initial porosities resulting from varying calendering degrees were perforated with short-pulsed laser radiation. Using SEM, strong calendering was found to result in superficial pore clogging, which was partly released by laser structuring. Agglomerations of the CMC on the electrode surfaces coming from re-deposited evaporated material were observed in an EDX analysis. An increase in the thickness and porosity of graphite anodes due to laser structuring was attributed to the removal of material and spring-back of the electrodes induced by the laser processing. Mercury porosimetry revealed a decrease of the prevalent pore sizes caused by calendering, but no further impact of laser structuring on the microstructure. Fitting of a transmission-line model to the impedance spectra of symmetric battery cells under blocking conditions revealed a strong increase of the ionic resistance and tortuosity with decreasing porosity. The effect is due to diffusion limitations caused by the electrode compression and was significantly diminished by laser structuring. In discharge rate tests, reduced capacities were obtained for LIBs at high C-rates between 1 C and 5 C. Strong calendering resulted in decreased discharge capacities at high currents. Laser structuring of the electrodes improved the discharge performance at high C-rates with a shift of the maximum performance improvement towards lower C-rates for decreasing bulk porosity. Even though the porosities and thicknesses of the electrodes were increased by laser structuring, structured anodes still outperformed the unstructured anodes in terms of capacity density and energy density.

In conclusion, a sweet spot for the application of electrode structuring in terms of the electrode bulk porosity and C-rate was identified in this study. The findings are of value for commercial manufacturers of LIBs and researchers, who wish to tune electrode properties via calendering and structuring. For an application of electrode structuring in industrial battery production, future research will need to focus on the inter-dependencies of laser structuring with other battery manufacturing processes such as coating or drying and an integration into the electrode manufacturing process chain. From the results of EDX and EIS analyses, a significant influence of the binder on the ablation behavior during laser electrode structuring as well as the resulting electrode properties was concluded in this study. Hence, laser structuring might affect the share and distribution of binder in the remaining electrode coating influencing the electrode's mechanical properties. Although it could be proven in the past that industrial processing of laser structured graphite anodes is feasible,[24,25] special attention has to be paid to the mechanical integrity of structured electrodes. The chemical state of the binder, which could also affect the LIB performance, will be studied in detail in future studies.

Acknowledgments

The authors thank David Schreiner and Moritz Kupec for the calendering of the electrodes. The financial support by the German Federal Ministry of Education and Research (BMBF) under the grant number 03XP03316B (LaserScale) is gratefully acknowledged.

Appendix

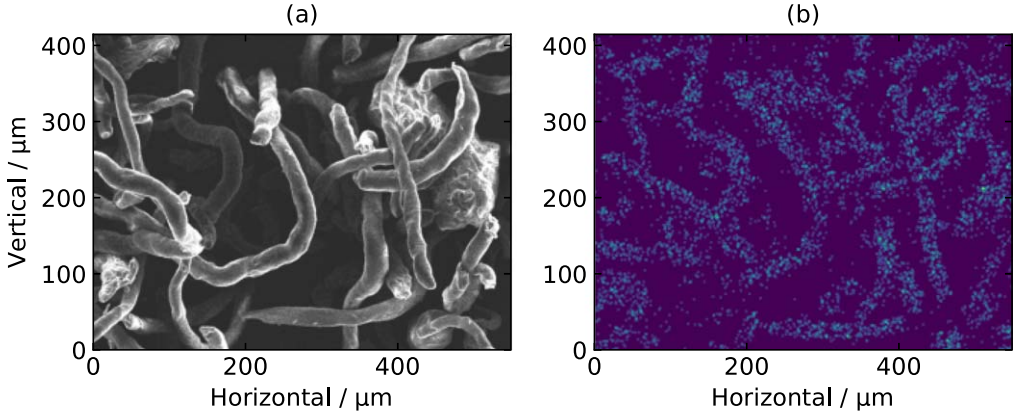

Figure A·1. (a) SEM image of pristine CMC and (b) the corresponding EDX map of sodium in normalized counts.

Table A·1. Test protocol for the C-rate test of full cells. The charging currents were increased at discharge C-rates larger than 1 C to reduce experiment time and repetitions were increased to evaluate degradations as well as residual effects from previous cycles.

Step	Description	Stopping conditions	Data registration	Repetitions
Charge	CC @ 0.1 C	$U>$ 4.2 V	$t=$ 30 s; $U=$ 10 mV	
Charge	CV @ 4.2 V	$t>$ 120 min; $I<$ 0.05 C	$t=$ 30 s; $U=$ 10 mV	3
Discharge	CC @ 0.1 C	$U<$ 2.9 V	$t=$ 30 s; $U=$ 10 mV	
Charge	CC @ 0.1 C	$U>$ 4.2 V	$t=$ 30 s; $U=$ 10 mV	
Charge	CV @ 4.2 V	$t>$ 120 min; $I<$ 0.05 C	$t=$ 30 s; $U=$ 10 mV	3
Discharge	CC @ 0.2 C	$U<$ 2.9 V	$t=$ 30 s; $U=$ 10 mV	
Charge	CC @ 0.1 C	$U>$ 4.2 V	$t=$ 30 s; $U=$ 10 mV	
Charge	CV @ 4.2 V	$t>$ 120 min; $I<$ 0.05 C	$t=$ 30 s; $U=$ 10 mV	3
Discharge	CC @ 0.5 C	$U<$ 2.9 V	$t=$ 30 s; $U=$ 10 mV	
Charge	CC @ 1 C	$U>$ 4.2 V	$t=$ 3 s; $U=$ 10 mV	
Charge	CV @ 4.2 V	$t>$ 120 min; $I<$ 0.05 C	$t=$ 3 s; $U=$ 10 mV	5
Discharge	CC @ 1 C	$U<$ 2.9 V	$t=$ 3 s; $U=$ 10 mV	
Charge	CC @ 1 C	$U>$ 4.2 V	$t=$ 3 s; $U=$ 10 mV	
Charge	CV @ 4.2 V	$t>$ 120 min; $I<$ 0.05 C	$t=$ 3 s; $U=$ 10 mV	5
Discharge	CC @ 2 C	$U<$ 2.9 V	$t=$ 3 s; $U=$ 10 mV	
Charge	CC @ 1 C	$U>$ 4.2 V	$t=$ 3 s; $U=$ 10 mV	
Charge	CV @ 4.2 V	$t>$ 120 min; $I<$ 0.05 C	$t=$ 3 s; $U=$ 10 mV	5
Discharge	CC @ 3 C	$U<$ 2.9 V	$t=$ 3 s; $U=$ 10 mV	
Charge	CC @ 1 C	$U>$ 4.2 V	$t=$ 3 s; $U=$ 10 mV	
Charge	CV @ 4.2 V	$t>$ 120 min; $I<$ 0.05 C	$t=$ 3 s; $U=$ 10 mV	5
Discharge	CC @ 4 C	$U<$ 2.9 V	$t=$ 3 s; $U=$ 10 mV	
Charge	CC @ 1 C	$U>$ 4.2 V	$t=$ 3 s; $U=$ 10 mV	
Charge	CV @ 4.2 V	$t>$ 120 min; $I<$ 0.05 C	$t=$ 3 s; $U=$ 10 mV	5
Discharge	CC @ 5 C	$U<$ 2.9 V	$t=$ 3 s; $U=$ 10 mV	
Charge	CC @ 0.1 C	$U>$ 4.2 V	$t=$ 30 s; $U=$ 10 mV	
Charge	CV @ 4.2 V	$t>$ 120 min; $I<$ 0.05 C	$t=$ 30 s; $U=$ 10 mV	3
Discharge	CC @ 0.1 C	$U<$ 2.9 V	$t=$ 30 s; $U=$ 10 mV	

ORCID

Lucas Hille https://orcid.org/0000-0001-5723-9408
Johannes Kriegler https://orcid.org/0000-0002-7961-7876
Josef Keilhofer https://orcid.org/0000-0002-5092-1567

References

1. C. Xu, Q. Dai, L. Gaines, M. Hu, A. Tukker, and B. Steubing, *Communications Materials*, **1** (2020).
2. J. Zhang, Z. Wang, P. Liu, and Z. Zhang, *Appl. Energy*, **275**, 115408 (2020).
3. S. Choi and G. Wang, *Adv. Mater. Technol.*, **3**, 1700376 (2018).
4. D. Andre, H. Hain, P. Lamp, F. Maglia, and B. Stiaszny, *J. Mater. Chem. A*, **5**, 17174 (2017).
5. K. G. Gallagher et al., *J. Electrochem. Soc.*, **163**, A138 (2015).
6. W. Haselrieder, S. Ivanov, D. K. Christen, H. Bockholt, and A. Kwade, *ECS Trans.*, **50**, 59 (2013).
7. H. Zheng, L. Tan, G. Liu, X. Song, and V. S. Battaglia, *J. Power Sources*, **208**, 52 (2012).
8. N. Billot, T. Günther, D. Schreiner, R. Stahl, J. Kranner, M. Beyer, and G. Reinhart, *Energy Technology*, **8**, 1801136 (2020).
9. T. Günther, D. Schreiner, A. Metkar, C. Meyer, A. Kwade, and G. Reinhart, *Energy Technology*, **8**, 1900026 (2020).
10. G. Lenze, F. Röder, H. Bockholt, W. Haselrieder, A. Kwade, and U. Krewer, *J. Electrochem. Soc.*, **164**, A1223 (2017).
11. C. Wang, Y. B. Yi, A. Sastry, J. Shim, and K. A. Striebel, *J. Electrochem. Soc.*, **6**, A1489 (2003).
12. B. Suthar, P. W. C. Northrop, D. Rife, and V. R. Subramanian, *J. Electrochem. Soc.*, **162**, A1708 (2015).
13. K. M. Abraham, *Electrochim. Acta*, **38**, 1233 (1993).
14. D. A. G. Bruggeman, *Ann. Phys.*, **416**, 636 (1935).
15. K. K. Patel, J. M. Paulsen, and J. Desilvestro, *J. Power Sources*, **122**, 144 (2003).
16. I. V. Thorat, D. E. Stephenson, N. A. Zacharias, K. Zaghib, J. N. Harb, and D. R. Wheeler, *J. Power Sources*, **188**, 592 (2009).
17. J. Landesfeind, A. Ehrl, M. Graf, W. A. Wall, and H. A. Gasteiger, *J. Electrochem. Soc.*, **163**, A1254 (2016).
18. V. P. Nemani, S. J. Harris, and K. C. Smith, *J. Electrochem. Soc.*, **162**, A1415 (2015).
19. J. B. Habedank, L. Kraft, A. Rheinfeld, C. Krezdorn, A. Jossen, and M. F. Zaeh, *J. Electrochem. Soc.*, **165**, A1563 (2018).
20. L. Kraft, J. B. Habedank, A. Frank, A. Rheinfeld, and A. Jossen, *J. Electrochem. Soc.*, **167**, 13506 (2020).
21. J. B. Habedank, J. Endres, P. Schmitz, M. F. Zaeh, and H. P. Huber, *J. Laser Appl.*, **30**, 32205 (2018).
22. M. Mangang, H. J. Seifert, and W. Pfleging, *J. Power Sources*, **304**, 24 (2016).
23. R. Dubey, M.-D. Zwahlen, Y. Shynkarenko, S. Yakunin, A. Fuerst, M. V. Kovalenko, and K. V. Kravchyk, *Batteries & Supercaps*, **4**, 464 (2021).
24. J. Kriegler, L. Hille, S. Stock, L. Kraft, J. Hagemeister, J. B. Habedank, A. Jossen, and M. F. Zaeh, *Appl. Energy*, **303**, 117693 (2021).
25. K.-H. Chen et al., *J. Power Sources*, **471**, 228475 (2020).
26. L. Hille, L. Xu, J. Keilhofer, S. Stock, J. Kriegler, and M. F. Zaeh, *Electrochim. Acta*, **392**, 139002 (2021).
27. J. Park, C. Jeon, W. Kim, S.-J. Bong, S. Jeong, and H.-J. Kim, *J. Power Sources*, **482**, 228948 (2021).
28. J. Pröll, H. Kim, A. Piqué, H. J. Seifert, and W. Pfleging, *J. Power Sources*, **255**, 116 (2014).
29. D. G. Lim, D.-W. Chung, R. Kohler, J. Proell, C. Scherr, W. Pfleging, and R. E. García, *J. Electrochem. Soc.*, **161**, A302 (2014).
30. W. Pfleging and P. Gotcu, *Applied Sciences*, **9**, 3588 (2019).
31. J. Park, S. Hyeon, S. Jeong, and H.-J. Kim, *J. Ind. Eng. Chem.*, **70**, 178 (2019).
32. P. Zhu, H. J. Seifert, and W. Pfleging, *Applied Sciences*, **9**, 4067 (2019).
33. Z. Song, P. Zhu, W. Pfleging, and J. Sun, *Nanomaterials*, **11**, 2962 (2021).
34. T. Tsuda, N. Ando, S. Nakamura, Y. Ishihara, N. Hayashi, N. Soma, T. Gunji, T. Tanabe, T. Ohsaka, and F. Matsumoto, *Electrochim. Acta*, **296**, 27 (2019).
35. D. L. Wood, J. Li, and C. Daniel, *J. Power Sources*, **275**, 234 (2015).
36. J. B. Habedank, F. J. Günter, N. Billot, R. Gilles, T. Neuwirth, G. Reinhart, and M. F. Zaeh, *Int. J. Adv. Manuf. Technol.*, **102**, 2769 (2019).
37. W. Pfleging and J. Pröll, *J. Mater. Chem. A*, **2**, 14918 (2014).
38. M.-J. Kleefoot, S. Enderle, J. Sandherr, M. Bolsinger, T. Maischik, N. Simon, J. Martan, S. Ruck, V. Knoblauch, and H. Riegel, *Int J Adv Manuf Technol*, **118**, 1987 (2021).
39. M. G. Berhe and D. Lee, *Micromachines*, **12**, 582 (2021).
40. T. Marks, S. Trussler, A. J. Smith, D. Xiong, and J. R. Dahn, *J. Electrochem. Soc.*, **158**, A51 (2011).
41. L. Froboese, P. Titscher, B. Westphal, W. Haselrieder, and A. Kwade, *Mater. Charact.*, **133**, 102 (2017).
42. D. Schreiner et al., *J. Electrochem. Soc.*, **168**, 30507 (2021).
43. J. Landesfeind, J. Hattendorff, A. Ehrl, W. A. Wall, and H. A. Gasteiger, *J. Electrochem. Soc.*, **163**, A1373 (2016).
44. M. Kroll, D. Hlushkou, S. Schlabach, A. Höltzel, B. Roling, and U. Tallarek, *J. Electrochem. Soc.*, **165**, A3156 (2018).

45. N. Ogihara, S. Kawauchi, C. Okuda, Y. Itou, Y. Takeuchi, and Y. Ukyo, *J. Electrochem. Soc.*, **159**, A1034 (2012).
46. R. Morasch, J. Keilhofer, H. A. Gasteiger, and B. Suthar, *J. Electrochem. Soc.*, **168**, 80519 (2021).
47. B. Schmieder, *Laser-based Micro- and Nanoprocessing*, ed. U. Klotzbach et al. (SPIE, San Francisco) IX (2015), 93511C.
48. S. Enderle, M. Bolsinger, S. Ruck, V. Knoblauch, and H. Riegel, *J. Laser Appl.*, **32**, 42008 (2020).
49. C. Meyer, H. Bockholt, W. Haselrieder, and A. Kwade, *J. Mater. Process. Technol.*, **249**, 172 (2017).
50. M. Ebner, D.-W. Chung, R. E. García, and V. Wood, *Adv. Energy Mater.*, **4**, 1301278 (2014).
51. M. Ebner and V. Wood, *J. Electrochem. Soc.*, **162**, A3064 (2014).
52. J. Landesfeind, A. Eldiven, and H. A. Gasteiger, *J. Electrochem. Soc.*, **165**, A1122 (2018).
53. M. Bolsinger, M. Weller, S. Ruck, P. Kaya, H. Riegel, and V. Knoblauch, *Electrochim. Acta*, **330**, 135163 (2020).
54. J. Landesfeind, M. Ebner, A. Eldiven, V. Wood, and H. A. Gasteiger, *J. Electrochem. Soc.*, **165**, A469 (2018).
55. J. B. Habedank, J. Kriegler, and M. F. Zaeh, *J. Electrochem. Soc.*, **166**, A3940 (2019).
56. C. Heubner, M. Schneider, and A. Michaelis, *Adv. Energy Mater.*, **10**, 1902523 (2020).
57. S. Schweidler, L. de Biasi, A. Schiele, P. Hartmann, T. Brezesinski, and J. Janek, *J. Phys. Chem. C*, **122**, 8829 (2018).
58. J. S. Kim, W. Pfleging, R. Kohler, H. J. Seifert, T. Y. Kim, D. Byun, H.-G. Jung, W. Choi, and J. K. Lee, *J. Power Sources*, **279**, 13 (2015).